

FINDING THE STRONGEST STABLE MASSLESS COLUMN WITH A FOLLOWER LOAD AND RELOCATABLE CONCENTRATED MASSES

by Oleg N. Kirillov and Michael L. Overton

(Northumbria University, Newcastle upon Tyne, NE1 8ST, UK.
Email: oleg.kirillov@northumbria.ac.uk)

(Courant Institute of Mathematical Sciences, New York University,
New York, NY, 10012, USA. Email: mo1@nyu.edu)

[August 2020 (original submission), February 2021 (revised submission)]

Summary

We consider the problem of optimal placement of concentrated masses along a massless elastic column that is clamped at one end and loaded by a nonconservative follower force at the free end. The goal is to find the largest possible interval such that the variation in the loading parameter within this interval preserves stability of the structure. The stability constraint is nonconvex and nonsmooth, making the optimization problem quite challenging. We give a detailed analytical treatment for the case of two masses, arguing that the optimal parameter configuration approaches the flutter and divergence boundaries of the stability region simultaneously. Furthermore, we conjecture that this property holds for any number of masses, which in turn suggests a simple formula for the maximal load interval for n masses. This conjecture is strongly supported by extensive computational results, obtained using the recently developed open-source software package GRANSO (GRadient-based Algorithm for Non-Smooth Optimization) to maximize the load interval subject to an appropriate formulation of the nonsmooth stability constraint. We hope that our work will provide a foundation for new approaches to classical long-standing problems of stability optimization for nonconservative elastic systems arising in civil and mechanical engineering.

1. Introduction

Consider an elastic Euler-Bernoulli beam clamped at one end and loaded at the tip by a follower force (1, 2). The follower force is defined as a force with the line of action that always coincides with the tangent line to the neutral axis of the deformed beam at its free end, much like a rocket thrust (3). The follower force does not depend on the velocity of the beam. However, it cannot be derived from a potential: the work done by the follower force along a closed contour is non-zero (4, 5). This structure is frequently called the Beck column (1, 2). A straight form of the Beck column is in a stable equilibrium when the follower force is absent or relatively small. Nevertheless, at some sufficiently large value the follower force excites exponentially growing oscillations of the beam that are known as flutter instability (6, 7).

Flutter is critically important both for safety of engineering structures interacting with fluid flows and for efficiency of energy harvesting devices that are based on the fluid-structure interactions. Recent years have seen an increasing interest in the Beck column in the modelling of biological filaments and their artificial biomimetic analogues, i.e., hair-like slender microscale structures that play an important part in such biological processes as swimming, pumping, mixing, and cytoplasmic streaming by performing rhythmic, wave-like motion that usually sets in via flutter instability (8, 9, 10, 11, 12).

Structural optimization of the Beck column against instabilities, including flutter and buckling (or divergence instability), is usually formulated as a problem on a redistribution of the material of the column of a given density under an isoperimetric constraint fixing the volume of the column in order to maximize the range of variation of the follower load corresponding to the stable structure. In the literature many specific numerically optimized shapes of the Beck column have been reported (29, 30, 31, 32, 33, 34) with the maximal critical dimensionless load reaching the values of $p \approx 100.00$ (33), $p \approx 139.30$ (35), $p \approx 143.59$ (36), and $p \approx 148.62$ (37), which significantly improve upon the critical load $p \approx 20.05$ of the uniform column with a constant cross-section (see Appendix A for the definition of p). Nevertheless, none of these designs is proven to be a global or even a local optimizer. Such a proof would be difficult to obtain because the problem of structural optimization of the critical flutter load for the elastic Beck column is both nonconvex and nonsmooth (38, 39).

Indeed, the elastic Beck column is a time-reversible dynamical system in which the transition from stability to flutter instability generically happens via the reversible-Hopf bifurcation, i.e., through the formation of a double imaginary eigenvalue with a Jordan block at the stability boundary and its subsequent splitting when parameters enter the instability region (40). Codimension-1 parts of the stability boundary are thus smooth hypersurfaces corresponding to double imaginary eigenvalues with a Jordan block (provided that the remaining eigenvalues are simple and imaginary) (7, 41, 42). These hypersurfaces can meet each other at sets of higher codimension such as intersections, cuspidal edges and points, conical points etc.; see (7) for a full classification of generic singularities on the stability boundary of mechanical systems with non-potential positional forces. The unavoidable singularities linked to multiple eigenvalues is the main reason for nonsmoothness of the merit functionals in the optimization of such systems, including the Beck column, with respect to stability criteria (43, 44).

Many studies report on the phenomenon of overlapping of eigenvalue curves that accompanies the process of optimization of the Beck column. The eigenfrequencies plotted as functions of the load exhibit sudden crossings during the optimization that lead to transfer of instability between modes and to a discontinuous change in the merit functional (17, 30, 31, 32, 33, 34, 36, 37, 45, 46, 47). The high sensitivity of the optimized design to variation of parameters is caused by the nonconvexity of the stability domain (38, 39). For this reason the unambiguous determination of the optimal design of the Beck column by numerical procedures typically used in civil and mechanical engineering remains a challenge (33, 36, 37).

All of the phenomena described above were also observed in simplified settings with the uniform Beck column carrying relocatable lumped masses (24, 47, 48, 49, 50, 51, 52, 53). Nevertheless, to the best of our knowledge, no rigorously proven local or global optimal

solutions or credible numerical guesses exist in the literature even in the problems of optimal localization of point masses along elastic beams loaded by the follower force.

Structures loaded by follower forces have long been questioned for their practical realization (13, 14), despite an evident example given by flexible missiles (15, 16, 17). In the 1970-90s, Sugiyama et al. used solid rocket motors to demonstrate flutter of cantilevers under a follower thrust on relatively short (several seconds) time intervals (3, 18, 19). A mechanism recently invented by Bigoni and Noselli produces a frictional follower force (20, 54) and enables experimental realization of fluttering cantilevered rods under follower loads on virtually infinite time intervals (21, 22). These practical realizations differ from the classical Beck column, however, by the presence of a finite-size loading unit at the tip of the cantilever and therefore are better described by the model of the Pflüger column (23, 24), which is the Beck column with a point mass at the loaded end; see the left panel of Fig. A in Appendix A.

In recent mechanical laboratory experiments with follower forces (21, 22), the ratio of the end mass to the mass of the column was chosen to be very large, approaching the so-called Dzhanelidze limit corresponding to a massless column (6). The instability thresholds obtained in these experiments were in a very good agreement with the theoretical predictions based on the Pflüger model. In the Dzhanelidze limit, the mathematical model is reduced to a system of ordinary differential equations (55, 56, 57, 58). The works (6, 24, 47) considered stability of a massless Pflüger column with an additional relocatable mass. A recent work (58) corrected some of the results reported in (6) and proposed extending the model to incorporate several relocatable masses.

The primary purpose of our paper is to study this last variant, the Pflüger model in the Dzhanelidze massless limit with relocatable point masses, in detail. One reason is that this comparatively simple but still mechanically meaningful model allows a detailed analytical treatment of the case of two masses, providing a benchmark for numerical optimization carried out for n masses. A second advantage of studying the discrete mass model instead of the classical Beck column is that it does not require Galerkin or finite element discretization, and hence the number of optimization variables is small (only $2n - 1$). Nonetheless, the problem of maximizing the load interval subject to the stability constraint is far from trivial because of the nonconvexity and nonsmoothness (in fact, non-Lipschitzness) of the constraint, so even this simplified model provides a good test of how much insight we can obtain using nonsmooth optimization techniques. Our first contribution, presented in Section 3, is to give a detailed analytical treatment for the case of two masses, arguing that the optimal parameter configuration approaches the flutter and divergence boundaries simultaneously. Furthermore, we conjecture that this property holds for any number of masses, which in turn suggests a simple formula for the optimal load interval for n masses. Our second contribution, in Section 4, is to present a practical numerical formulation of the stability constraint and to maximize the load interval subject to this constraint using modern techniques for nonsmooth, nonconvex optimization, employing a recently developed open-source software package, GRANSO (GRAdient-based Algorithm for Non-Smooth Optimization) (59, 60). As well as verifying our analytical solution for two masses, these computations strongly support the formula for the conjectured optimal load interval for n masses. We hope that our techniques and results will provide a foundation and inspiration for new approaches to classical long-standing problems of stability optimization for nonconservative elastic systems arising in civil and mechanical engineering.

2. A massless elastic column with n concentrated masses

It is convenient to first consider the simple model of the Pflüger column without relocatable masses, with zero mass per unit length and zero point mass at the free end of the column (see Appendix A for details). Then, the boundary value problem (A.5), (A.6) takes the form

$$\partial_\xi^4 f + \kappa^2 \partial_\xi^2 f = 0, \quad (2.1)$$

$$f(0) = 0, \quad \partial_\xi f(0) = 0, \quad \partial_\xi^2 f(1) = 0, \quad \partial_\xi^3 f(1) = 0, \quad (2.2)$$

where

$$\kappa^2 = p, \quad (2.3)$$

with p given in (A.4).

Following (6, 24, 58), consider the case when a concentrated constant force F is acting in a direction perpendicular to the non-deformed column at the point $s = \alpha l$. Introducing the dimensionless version of the force parameter, $\phi = \frac{Fl^2}{ET}$, we seek the general solution to the equation (2.1) in the form (6, 24, 58)

$$f(\xi) = u(\xi) + \begin{cases} 0, & \xi \in [0, \alpha) \\ v(\xi), & \xi \in [\alpha, 1] \end{cases} \quad (2.4)$$

where

$$u(\xi) = A \sin \kappa \xi + B \cos \kappa \xi + C \xi + D$$

and

$$v(\xi) = A_1 \sin \kappa \xi + B_1 \cos \kappa \xi + C_1 \xi + D_1.$$

To determine the coefficients A_1 , B_1 , C_1 , and D_1 , we require that

$$\begin{aligned} u(\alpha) &= f(\alpha), & \partial_\xi u(\alpha) &= \partial_\xi f(\alpha), \\ \partial_\xi^2 u(\alpha) &= \partial_\xi^2 f(\alpha), & \partial_\xi^3 f(\alpha) - \partial_\xi^3 u(\alpha) &= \phi. \end{aligned} \quad (2.5)$$

This yields

$$v(\xi) = \frac{(\xi - \alpha)\kappa - \sin((\xi - \alpha)\kappa)}{\kappa^3} \phi. \quad (2.6)$$

Taking (2.6) into account in the general solution (2.4) and then substituting $f(\xi)$ into the boundary conditions (2.2), we find the coefficients A , B , C , and D to obtain

$$u(\xi) = \frac{\sin(\kappa \alpha) - \xi \kappa \cos(\kappa \alpha) + \sin((\xi - \alpha)\kappa)}{\kappa^3} \phi. \quad (2.7)$$

Let us now assume that the massless cantilevered column loaded by the follower force at its free end carries n concentrated masses with the mass $M_n > 0$ fixed at the loaded end; see Fig. 1. The masses $M_i \geq 0$, $i = 1, \dots, n-1$, are located at the distances $s_i < l$ from the clamped end of the column. Let v_i be a transversal displacement of the mass M_i from the equilibrium configuration, as shown in Fig. 1. Introducing the dimensionless displacements of the masses, w_i , the distances, α_i , and the mass ratios, μ_i , as

$$w_i = \frac{v_i}{l}, \quad \alpha_i = \frac{s_i}{l}, \quad \mu_i = \frac{M_i}{M_n}, \quad i = 1, \dots, n, \quad (2.8)$$

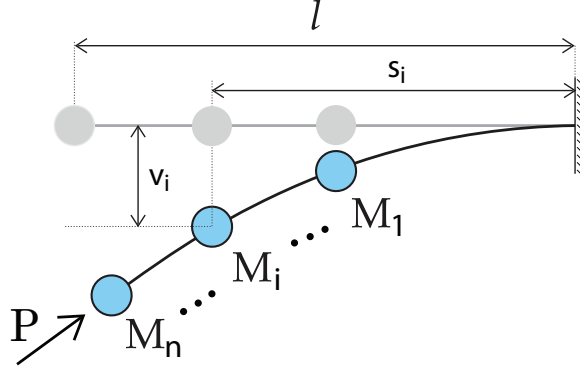


Fig. 1 The massless Beck column loaded by the follower force P with n concentrated masses $M_1, \dots, M_i, \dots, M_n$ attached (53, 58).

we write the equations of motion of the masses (6, 24, 58)

$$\begin{aligned}
 w_1 &= -\gamma_{11}\mu_1 \frac{d^2 w_1}{d\tau^2} - \gamma_{12}\mu_2 \frac{d^2 w_2}{d\tau^2} - \dots - \gamma_{1n}\mu_n \frac{d^2 w_n}{d\tau^2}, \\
 w_2 &= -\gamma_{21}\mu_1 \frac{d^2 w_1}{d\tau^2} - \gamma_{22}\mu_2 \frac{d^2 w_2}{d\tau^2} - \dots - \gamma_{2n}\mu_n \frac{d^2 w_n}{d\tau^2}, \\
 &\vdots \\
 w_i &= -\gamma_{i1}\mu_1 \frac{d^2 w_1}{d\tau^2} - \gamma_{i2}\mu_2 \frac{d^2 w_2}{d\tau^2} - \dots - \gamma_{in}\mu_n \frac{d^2 w_n}{d\tau^2}, \\
 &\vdots \\
 w_n &= -\gamma_{n1}\mu_1 \frac{d^2 w_1}{d\tau^2} - \gamma_{n2}\mu_2 \frac{d^2 w_2}{d\tau^2} - \dots - \gamma_{nn}\mu_n \frac{d^2 w_n}{d\tau^2},
 \end{aligned} \tag{2.9}$$

where the dimensionless time τ is defined now as

$$\tau = t \sqrt{\frac{EI}{M_n l^3}}. \tag{2.10}$$

Note that $\alpha_1 \leq \alpha_2 \leq \dots \leq \alpha_n = 1$ and $\mu_n = 1$. The coefficient γ_{ij} is the displacement of the mass μ_i as a result of application to the column of a unit force $\phi = 1$ at the point α_j . According to (2.4) with the functions (2.6) and (2.7) the coefficient γ_{ij} is given by δ_{ij}/κ^3 , where

$$\begin{aligned}
 \delta_{ij} &= \sin(\kappa\alpha_j) - \alpha_i \kappa \cos(\kappa\alpha_j) + \sin((\alpha_i - \alpha_j)\kappa) \\
 &+ \begin{cases} 0, & i \leq j \\ (\alpha_i - \alpha_j)\kappa - \sin((\alpha_i - \alpha_j)\kappa), & i > j. \end{cases}
 \end{aligned} \tag{2.11}$$

Separating time with the ansatz $w_i = u_i e^{\sigma \kappa^{3/2} \tau}$ we arrive at the eigenvalue problem

$$(\mathbf{M}\sigma^2 + \mathbf{K})u = 0, \tag{2.12}$$

where $u = (u_1, u_2, \dots, u_n)$, \mathbf{K} is the $n \times n$ unit matrix, and

$$\mathbf{M} = \begin{pmatrix} \mu_1 \delta_{11} & \mu_2 \delta_{12} & \cdots & \mu_n \delta_{1n} \\ \mu_1 \delta_{21} & \mu_2 \delta_{22} & \cdots & \mu_n \delta_{2n} \\ \vdots & \vdots & \ddots & \vdots \\ \mu_1 \delta_{n1} & \mu_2 \delta_{n2} & \cdots & \mu_n \delta_{nn} \end{pmatrix}, \quad (2.13)$$

where, as already noted, $\mu_n = 1$. The eigenvalues σ_k are given by

$$\sigma_k = \pm \sqrt{-\lambda_k^{-1}} \quad (2.14)$$

where the λ_k are the eigenvalues of the matrix \mathbf{M} .

The trivial equilibrium of the circulatory system (2.9) is stable if and only if the eigenvalues σ_k are imaginary and semisimple (i.e., the algebraic and geometric multiplicity are equal), or equivalently, the λ_k are real, positive and semisimple. Cases with a multiple imaginary eigenvalue σ_k with a Jordan block (i.e., with the algebraic multiplicity exceeding the geometric multiplicity) lie on the boundary between the stability and flutter domains. In the generic case the crossing of this stability boundary is accompanied by merging of two simple imaginary eigenvalues into a double imaginary eigenvalue with a Jordan block, indicating the onset of the reversible-Hopf bifurcation or flutter (6, 7, 41, 42). Non-oscillatory instability or divergence corresponds to one or more positive real eigenvalues σ_k and in this model it generically sets in when two conjugate simple imaginary eigenvalues meet at infinity, split and turn back towards the origin along the real axis in the complex plane (26, 27, 58).

Summarizing, for a given number of masses n , the eigenvalue problem (2.12) is defined by (2.11) and (2.13), which depend on the given load κ and the parameters α_i and μ_i , $i = 1, \dots, n-1$, defined in (2.8) (as $\alpha_n = \mu_n = 1$). It is convenient to use the parameterization

$$\mu_i = \tan \beta_i, \quad \beta_i \in [0, \pi/2), \quad i = 1, \dots, n-1. \quad (2.15)$$

Given α_i, β_i , $i = 1, \dots, n-1$, let us define $\kappa_{\text{crit}}^{\alpha, \beta}$ as the largest value such that the eigenvalues σ_k (which depend on α_i , β_i and κ) are imaginary for all $\kappa \in [0, \kappa_{\text{crit}}^{\alpha, \beta}]$. Our goal is to find the supremum of $\kappa_{\text{crit}}^{\alpha, \beta}$ over all parameters $\alpha_i \in [0, 1]$ and $\beta_i \in [0, \pi/2)$, $i = 1, \dots, n-1$. We begin with the case $n = 2$, where we propose an analytical solution.

3. Analytical derivation of the supremal load interval for the massless column carrying two concentrated masses

When $n = 2$, the massless column carries a relocatable mass M_1 between the clamped end and the free end of the rod with mass M_2 fixed at the free end. There are two parameters, α_1 and β_1 . Expression (2.11) allows us to find the coefficients δ_{ij} in the explicit form, cf. (6, 58),

$$\begin{aligned} \delta_{11} &= \sin(\kappa \alpha_1) - \kappa \alpha_1 \cos(\kappa \alpha_1) \\ \delta_{12} &= \sin(\kappa) - \kappa \alpha_1 \cos(\kappa) - \sin(\kappa(1 - \alpha_1)) \\ \delta_{21} &= \sin(\kappa \alpha_1) - \kappa \cos(\kappa \alpha_1) + \kappa(1 - \alpha_1) \\ \delta_{22} &= \sin(\kappa) - \kappa \cos(\kappa). \end{aligned} \quad (3.1)$$

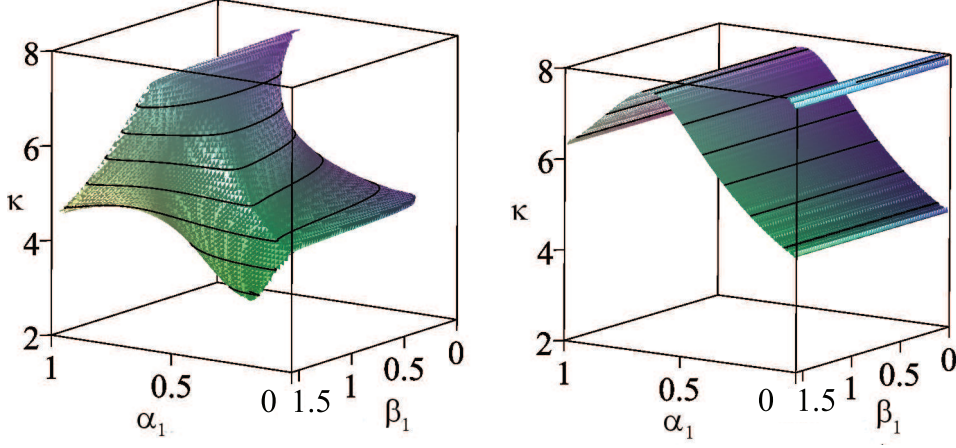


Fig. 2 The case of $n = 2$ concentrated masses. (Left) the flutter domain is a finite solid set in the $(\alpha_1, \beta_1, \kappa)$ space, enclosed within the singular surface defined by (3.4). (Right) The divergence domain lies above the boundary set defined by (3.3). For a given (α_1, β_1) , the critical value of the load parameter, $\kappa_{\text{crit}}^{\alpha_1, \beta_1}$, is the minimal value of κ that satisfies either (3.4) or (3.3), as this is the length of the longest vertical line segment rising from the point $(\alpha_1, \beta_1, 0)$ that does not enter either the flutter or divergence domain. Consequently, this is the largest value $\tilde{\kappa}$ such that the column is stable for all $\kappa \in [0, \tilde{\kappa}]$. The optimization problem to be solved is to find the supremum of $\kappa_{\text{crit}}^{\alpha_1, \beta_1}$ over all $\alpha_1 \in [0, 1]$, $\beta_1 \in [0, \pi/2]$.

As we will see, already in this simplest possible mechanical system, the subdivision of the parameter space into the domains of stability, flutter instability, and divergence instability is highly nontrivial. However, we will be able to explore it completely and find an apparent supremum of the critical load parameter defining the longest stability interval $[0, \kappa_{\text{crit}}^{\alpha_1, \beta_1}]$ in the space of parameters $\alpha_1 \in [0, 1]$, $\beta_1 \in [0, \pi/2]$.

In general, the stability map for a mechanical system with the characteristic polynomial $p(\sigma) = \det(\mathbf{M}\sigma^2 + \mathbf{K})$ can be obtained with the use of the Gallina criterion (7, 61, 62) that is based on the investigation of the discriminant of the polynomial. For $n = 2$, $p(\sigma)$ is a biquadratic function

$$\begin{aligned} p(\sigma) = & \sigma^4 \tan \beta_1 \{ \kappa(\alpha_1 - 1)(\sin \kappa - \kappa \alpha_1 \cos \kappa + \sin(\kappa \alpha_1 - \kappa)) \\ & - \sin(\kappa(\alpha_1 - 1))(\sin(\kappa \alpha_1) - \kappa \cos(\kappa \alpha_1) - \kappa(\alpha_1 - 1)) \} \\ & + \sigma^2 [\tan \beta_1 (\sin(\kappa \alpha_1) - \kappa \alpha_1 \cos(\kappa \alpha_1)) - \kappa \cos \kappa + \sin \kappa] + 1. \end{aligned} \quad (3.2)$$

Notice that the coefficient at the leading power of σ in the polynomial (3.2) is nothing else but $\det \mathbf{M}$; see (7). The system loses stability by divergence as soon as $\det \mathbf{M} = 0$, which yields the following equation determining the divergence boundary:

$$\frac{\sin \kappa - \kappa \alpha_1 \cos \kappa + \sin(\kappa \alpha_1 - \kappa)}{\sin(\kappa \alpha_1) - \kappa \cos(\kappa \alpha_1) - \kappa(\alpha_1 - 1)} = \frac{\sin(\kappa(\alpha_1 - 1))}{\kappa(\alpha_1 - 1)}. \quad (3.3)$$

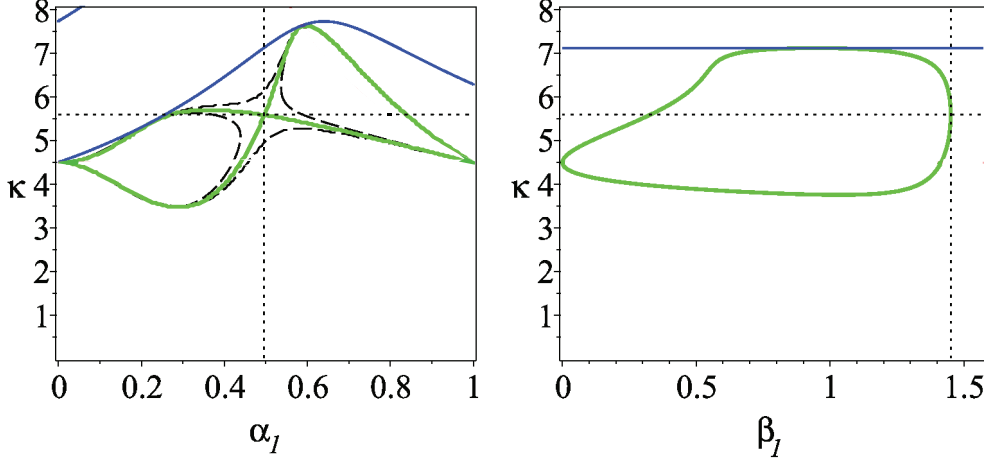


Fig. 3 Stability diagrams for (left) $\beta_1 = \hat{\beta} = 1.450234089$ in the (α_1, κ) -plane and (right) for $\alpha_1 = \hat{\alpha} = 0.4947347666$ in the (β_1, κ) -plane. The solid blue curves designate the divergence boundary (3.3) and the solid green curves mark the flutter boundary (3.4). The flutter boundary in the left panel has a crossing at the saddle point located at $\alpha_1 = \hat{\alpha}$ and $\kappa = 5.591633160$. The black dashed curves in the left panel correspond to the flutter boundaries at (upper and lower curves) $\beta_1 = \hat{\beta} - 0.01$ and (left and right curves) $\beta_1 = \hat{\beta} + 0.01$. In the right panel, the divergence boundary is a horizontal blue line with height $\kappa = \hat{\kappa} = 7.113918994$.

Note that this equation is independent of β_1 . The right panel of Fig. 2 shows the divergence boundary (3.3) in the $(\alpha_1, \beta_1, \kappa)$ -space.

The roots of the characteristic polynomial (3.2) are double imaginary if the discriminant of the biquadratic function vanishes:

$$\begin{aligned}
 & (\sin(\kappa\alpha_1) - \kappa\alpha_1 \cos(\kappa\alpha_1))^2 (\tan \beta_1)^2 \\
 & + 2\alpha_1 \kappa^2 \tan \beta_1 \cos \kappa [\cos(\kappa\alpha_1) + 2(\alpha_1 - 1)] \\
 & + 2 \tan \beta_1 \sin(\kappa\alpha_1) [2 \sin(\kappa(\alpha_1 - 1)) + \sin \kappa] \\
 & - \kappa \tan \beta_1 [7 \sin(\kappa(\alpha_1 - 1))(\alpha_1 - 1) + \sin(\kappa(\alpha_1 + 1))(\alpha_1 + 1)] \\
 & - 2\kappa \tan \beta_1 [(2\alpha_1 - 3) \sin \kappa + \sin(\kappa(2\alpha_1 - 1))] \\
 & + (\sin \kappa - \kappa \cos \kappa)^2 = 0.
 \end{aligned} \tag{3.4}$$

For this reason (6, 7, 42) equation (3.4) determines the boundary of the flutter domain that is shown in the left panel of Fig. 2.

For a given (α_1, β_1) , the critical value of the load parameter is given by

$$\kappa_{\text{crit}}^{\alpha_1, \beta_1} = \min\{\kappa : (\kappa, \alpha_1, \beta_1) \text{ satisfies either (3.3) or (3.4)}\},$$

as this is the length of the longest vertical line segment rising from the point $(\alpha_1, \beta_1, 0)$ that does not enter either the flutter or the divergence domain. Consequently, the quantity

$$\kappa^* = \sup\{\kappa_{\text{crit}}^{\alpha_1, \beta_1} : \alpha_1 \in [0, 1], \beta_1 \in [0, \pi/2)\} \tag{3.5}$$

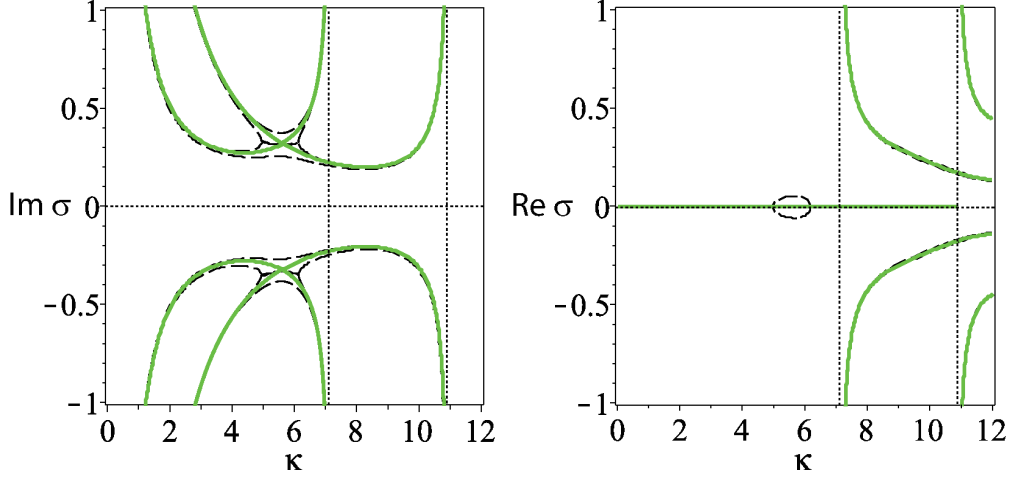


Fig. 4 (Left) imaginary and (right) real roots of the characteristic polynomial (3.2) for $\alpha_1 = \hat{\alpha} = 0.4947347666$ and (green, solid) $\beta_1 = \hat{\beta} = 1.450234089$ and (black, dashed) $\hat{\beta} \pm 0.01$. A bubble of complex eigenvalues appears for $\beta_1 = 1.450234089 - 0.01$ and corresponds to flutter instability. The black dotted vertical line at $\kappa = \hat{\kappa} = 7.113918994$ is the onset of divergence instability. Increase in β_1 from $\hat{\beta} - 0.01$ to $\hat{\beta} + 0.01$ results in the disappearance of the complex eigenvalues and hence is accompanied by the transition from the overlapping eigenvalue branches to an avoided crossing that yields a jump in the critical load parameter to the maximal value that is reached at $\kappa = \hat{\kappa}$ on the divergence boundary (58); see also the right panel of Fig. 3.

is the supremum of all loads associated with a stable column. Note that although the divergence boundary (3.3) is smooth, the boundary of the flutter domain (3.4) is nonsmooth.

Fig. 3 shows cross-sections of the flutter boundary and the divergence boundary in the (α_1, κ) - and (β_1, κ) -planes. In the left panel, for which β_1 is fixed to $\hat{\beta} \approx 1.45$, we see that the flutter boundary has a saddle point in the (α_1, κ) -plane at $\alpha_1 = \hat{\alpha} \approx 0.495$, $\kappa \approx 5.59$. On the other hand, when α_1 is fixed to $\hat{\alpha}$, the flutter boundary has a vertical tangent in the (β_1, κ) -plane at $\beta_1 = \hat{\beta}$, as is visible in the right panel of Fig. 3. Consequently, when $\alpha_1 = \hat{\alpha}$, the maximal stable load $\kappa_{\text{crit}}^{\alpha_1, \beta_1}$ varies smoothly for $\beta_1 \in (0, \hat{\beta})$, but when β_1 reaches $\hat{\beta}$ it jumps up discontinuously from the flutter boundary to the divergence boundary. For the system under study such jumps were first described in the work (58) that corrected the classical result of Bolotin (6), whose plot in the (β_1, κ) -plane did not contain the divergence boundary at all, but provided a correct shape for the flutter boundary. Notice that such overlapping of eigenvalue branches typically accompanies optimization of nonconservative systems and was reported in numerous studies (6, 17, 19, 27, 30, 31, 32, 33, 34, 35, 36, 37). The general theory of this effect has been developed in (7, 38, 39).

We can obtain a clearer picture of the jump discontinuity by plotting the real and imaginary parts of the eigenvalues σ which describe the flutter boundary, as is done in Fig. 4. For $\alpha_1 = \hat{\alpha}$, when β_1 is decreased from the value $\hat{\beta}$, a bubble of complex eigenvalues corresponding to flutter appears, but this vanishes for $\beta_1 \geq \hat{\beta}$, resulting in the transition of the critical load from the flutter boundary to the divergence boundary.

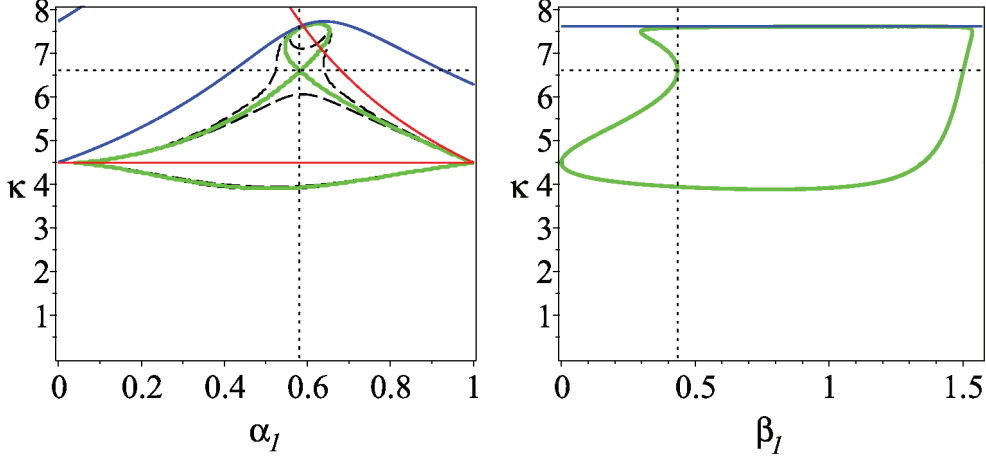


Fig. 5 Stability diagrams for (left) $\beta_1 = \tilde{\beta} = 0.4342999969$ in the (α_1, κ) -plane and (right) for $\alpha_1 = \tilde{\alpha} = 0.5810701268$ in the (β_1, κ) -plane. The solid blue curves designate the divergence boundary (3.3), and the solid green curves mark the flutter boundary (3.4). The flutter boundary in the left panel has a crossing at the saddle point located at $\alpha_1 = \tilde{\alpha}$ and $\kappa = 6.600674669$. The black dashed curves in the left panel correspond to the flutter boundaries at (upper and lower curves) $\beta_1 = \tilde{\beta} - 0.05$ and (left and right curves) $\beta_1 = \tilde{\beta} + 0.05$. In the right panel, the divergence boundary is the horizontal blue line with height $\kappa = 7.607584259$. The horizontal red line in the left panel shows the value κ_0 given in (3.8) which is the smallest positive root of (3.6): the flutter boundary for the case $\beta_1 = 0$. The other red solid curve in the left panel is the solution to (3.7): the flutter boundary for the case $\beta_1 = \pi/2$.

Looking at the discriminant (3.4) we notice that it degenerates into the equation

$$\kappa \cos(\kappa) - \sin(\kappa) = 0 \quad (3.6)$$

for $\beta_1 = 0$ (i.e., when $\mu_1 = 0$) and reduces to the equation

$$\sin(\kappa\alpha_1) - \kappa\alpha_1 \cos(\kappa\alpha_1) = 0 \quad (3.7)$$

in the limit $\beta_1 \rightarrow \pi/2$ (i.e., $\mu_1 \rightarrow \infty$). The sets defined by equations (3.6) and (3.7) are shown by the solid red line and curve, respectively, in the left panel of Fig. 5. The flutter boundary is tangent to the planes $\beta_1 = 0$ and $\beta_1 = \pi/2$ along this line and curve. Note that the height of the red line is the smallest positive root of (3.6), which we denote by κ_0 , with

$$\kappa_0 \approx 4.493409458. \quad (3.8)$$

Since $\beta_1 = 0$ is the case where the mass $M_1 = 0$, κ_0 is the square root of the critical load for the Dzhanelidze column (in view of (A.9) and (2.3)). The lines $\kappa = \kappa_0$ at $\alpha_1 = 0$ and $\alpha_1 = 1$ form singularities (edges) of the flutter domain.

As soon as β_1 starts deviating from zero, a closed region of flutter instability appears

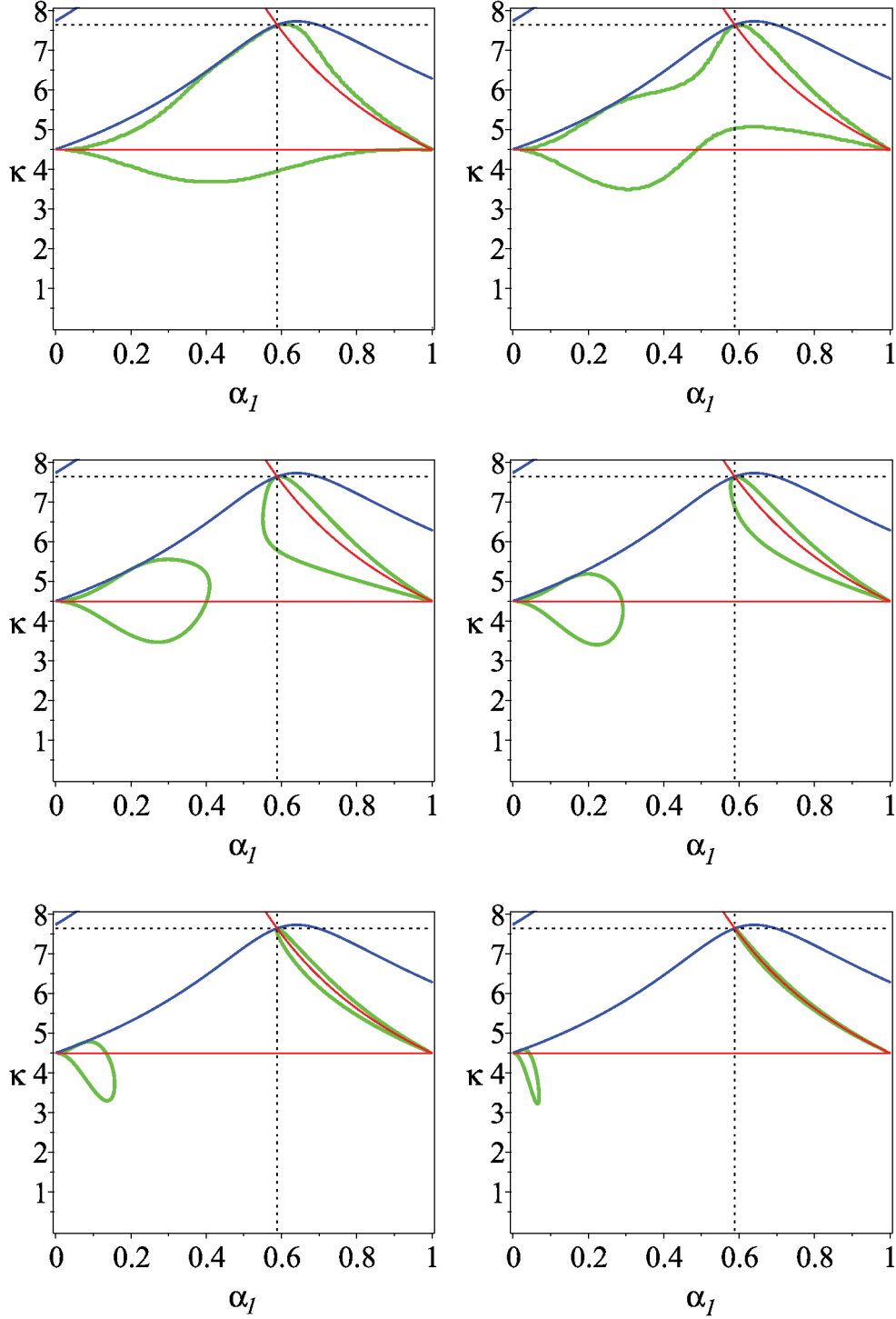


Fig. 6 Stability diagrams in the (α_I, κ) -plane for (upper left) $\beta_1 = \pi/2 - 0.5$, (upper right) $\beta_1 = \pi/2 - 0.15$, (middle left) $\beta_1 = \pi/2 - 0.1$, (middle right) $\beta_1 = \pi/2 - 0.05$, (lower left) $\beta_1 = \pi/2 - 0.01$, and (lower right) $\beta_1 = \pi/2 - 0.001$. The black dashed lines intersect at the point with the coordinates of the optimal solution: $\alpha_I^* \approx 0.588527598$ and $\kappa^* \approx 7.635002111$.

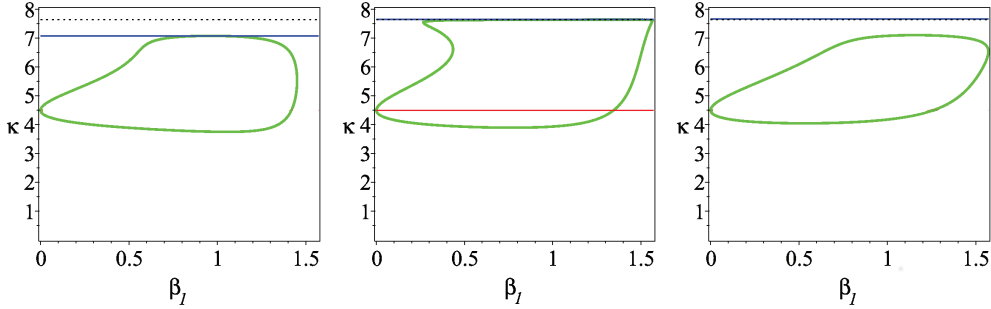


Fig. 7 Stability diagrams for (left) $\alpha_1 = \alpha_1^* - 0.1$, (center) $\alpha_1 = \alpha_1^* \approx 0.5885275986$ and (right) $\alpha_1 = \alpha_1^* + 0.1$. The green and blue curves respectively show the flutter and divergence boundaries. In the left and center panels, the critical load reaches the divergence boundary, but this is higher in the center panel, and there it is reached only if $\beta_1 = \pi/2$. In the right panel, the flutter boundary prevents the critical load from reaching the divergence boundary.

around the horizontal red line $\kappa = \kappa_0$ in the (α_1, κ) -plane. Furthermore, another region of flutter originates above it that touches the divergence boundary. These two regions coalesce when β_1 reaches $\tilde{\beta} \approx 0.434$; see the left panel of Fig. 5, which shows another resulting saddle point on the flutter boundary defined by (3.4). With further growth in β_1 the flutter region in the (α_1, κ) -plane is simply connected, as shown in the two upper panels of Fig. 6 corresponding to $\beta_1 = \pi/2 - 0.5$ and $\beta_1 = \pi/2 - 0.15$, respectively, until this parameter passes the value $\beta_1 \approx 1.45$, after which the flutter domain bifurcates into two parts; see the middle and the lower panels in Fig. 6.

As β_1 approaches $\pi/2$, the upper portion of the flutter region concentrates around the red curve defined by (3.7), as shown in the lower panels of Fig. 6, and coincides with this curve exactly at $\beta_1 = \pi/2$. At this very limit the critical load κ reaches its supremal value κ^* , defined in (3.5), which can be obtained by finding the intersection point of the red curve defined by (3.7) and blue curve defined by the divergence boundary (3.3). Solving the equations (3.3) and (3.7) simultaneously, we find

$$\kappa^* \approx 7.635002112, \quad \alpha_1^* \approx 0.5885275986, \quad (3.9)$$

and we write

$$\beta_1^* = \frac{\pi}{2} \quad (3.10)$$

to indicate that the supremum occurs in the limit $\beta_1 \rightarrow \pi/2$.

Stability diagrams in Fig. 7 presented in the (β_1, κ) -plane show the decrease in the critical load κ when α_1 deviates from the value α_1^* , indicating that the value κ^* is a local supremum in the parameter space $\alpha_1 \in [0, 1]$, $\beta_1 \in [0, \pi/2)$. Experiments reported in the next section strongly indicate that κ^* is actually the global supremum. However, note that \mathbf{M} is not defined at $\beta_1^* = \pi/2$, since then the mass ratio $\mu_1 = M_1/M_2$ is infinite, so the supremum is not attained. Furthermore, as $(\kappa, \alpha_1, \beta_1) \rightarrow (\kappa^*, \alpha_1^*, \pi/2)$, the matrix element \mathbf{M}_{21} diverges to ∞ and \mathbf{M}_{12} converges to 0 (see (3.3)), but \mathbf{M}_{11} is the product of two quantities, one diverging to ∞ and the other converging to 0 (see (3.7)). For this reason it is difficult

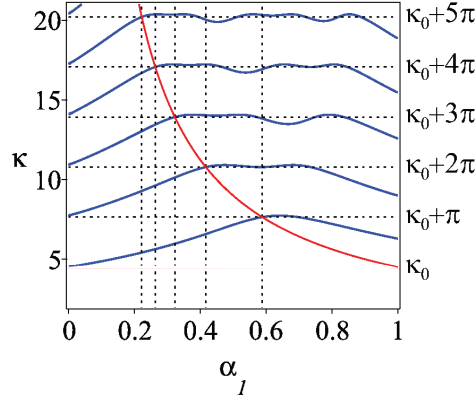


Fig. 8 Graphs of (red) equation (3.7) defining the flutter boundary in the limit $\beta_1 \rightarrow \pi/2$ as a function of α_1 and (blue) equation (3.3) defining the divergence boundary as a function of α_1 . The intersection points are given by the expressions (3.12) and (3.13).

to rigorously state limiting properties of the eigenvalues λ_k of \mathbf{M} as the supremum is approached, though based on both our symbolic and numerical calculations, it seems that, under the appropriate assumptions, the eigenvalues converge to a double zero eigenvalue with a Jordan block, indicating that the parameters are on the boundary of both the flutter and divergence domains, and that the limiting eigenvalues σ_k of (2.12) coalesce into a quadruple eigenvalue at ∞ .

A key point in the derivation above is that the supremal value of $\kappa_{\text{crit}}^{\alpha, \beta}$ occurs when the divergence boundary meets the flutter boundary in the limit $\beta_1 \rightarrow \pi/2$. We conjecture that this property holds for all n , not just for $n = 2$. If we substitute (3.7), which is the equation for the flutter boundary in the limit $\beta_1 \rightarrow \pi/2$, into the divergence boundary equation (3.3), the latter can be simplified and reduced to

$$\kappa(\alpha_1 - 1) \sin(\kappa(\alpha_1 - 1)) (\cos(\kappa\alpha_1) - 1)^2 = 0. \quad (3.11)$$

Writing $\sin(\kappa(\alpha_1 - 1)) = 0$ yields $\kappa\alpha_1 - \kappa + k\pi = 0$, $k \in \mathbb{Z}$. On the other hand, the relation (3.7) can be written as $\kappa\alpha_1 = \tan(\kappa\alpha_1)$, yielding $\kappa\alpha_1 = \kappa_0$, where κ_0 , given by (3.8), is the smallest positive root of the equation $\tan \kappa = \kappa$. Combining the results, we obtain $\kappa = \kappa_0 + \pi k$, with $k \in \mathbb{Z}$. For $k = 0$, we obtain $\kappa = \kappa_0$, the optimal load when the mass M_1 is absent (and the square root of the critical load for the Dzhanelidze column), while for $k = 1$, we obtain $\kappa = \kappa_0 + \pi$, the supremum in (3.9) just obtained for the optimal load for two concentrated masses M_1 and M_2 . Let us therefore set $k = n - 1$, giving

$$\kappa = \kappa_0 + (n - 1)\pi, \quad (3.12)$$

and hence, using $\kappa\alpha_1 = \kappa_0$,

$$\alpha_1 = \frac{\kappa_0}{\kappa_0 + (n - 1)\pi}. \quad (3.13)$$

For $n = 1$, the expression (3.13) yields $\alpha_1 = 1$, and for $n = 2$, we have $\alpha_1 = \kappa_0(\kappa_0 + \pi)^{-1}$,

which is the optimal value α_1^* given in (3.9). This suggests a conjecture that (3.12) and (3.13) are respectively the supremal value κ^* and the corresponding limiting value α_1^* for all n , with the corresponding limiting value β_1^* equal to $\pi/2$. Fig. 8 shows the values (3.12) and (3.13) as defined by the intersections of equations (3.3) and (3.7), the divergence boundary equation and the flutter boundary equation in the limit $\beta_1 = \pi/2$, respectively. (It's perhaps worth noting that, for all n , we have $\tan(\kappa_0 + (n-1)\pi) = \tan(\kappa_0) = \kappa_0$.)

Remarkably, the numerical computations reported in the next section for n concentrated masses, with $n = 2, 3, 4, 5$, strongly indicate that the supremal load κ^* and the corresponding limiting value α_1^* are precisely the values given in (3.12) and (3.13) and illustrated in Fig. 8, with the corresponding limiting value β_1^* equal to $\pi/2$. While we do not have conjectured formulas for the limiting values α_i^* for $i > 1$ and $n > 2$, we conjecture that the corresponding limiting values β_i^* are all $\pi/2$. Indeed, the property $\beta_1^* = \pi/2$ implies that the mass ratio $\mu_1 = M_1/M_n \rightarrow \infty$ as $\kappa \rightarrow \kappa^*$, which implies, assuming that M_1 is bounded above, that $M_n \rightarrow 0$. Consequently, if the other masses are nonzero in the limit, all mass ratios $\mu_i = M_i/M_n$ must diverge to infinity as $\kappa \rightarrow \kappa^*$.

4. Numerical derivation of the optimal load for the massless column carrying multiple relocatable masses

Recall that, as discussed in Section 2, for a given number of masses n , our stability constraint is defined by the eigenvalue problem $(\mathbf{M}\sigma^2 + \mathbf{K})u = 0$ (see (2.12)). Here \mathbf{K} is the unit matrix while \mathbf{M} is defined by (2.11) and (2.13), which depend on the dimensionless parameters α_i and $\mu_i = \tan \beta_i$, $i = 1, \dots, n-1$, defined in (2.8), as well as a given load κ . Let us write $\mathbf{M}(\alpha, \beta, \kappa)$ for the matrix \mathbf{M} defined by $\alpha = [\alpha_1, \dots, \alpha_{n-1}]^T$, $\beta = [\beta_1, \dots, \beta_{n-1}]^T$ and κ . As noted in (2.14), the eigenvalues σ_k of $(\mathbf{M}(\alpha, \beta, \kappa)\sigma^2 + \mathbf{K})u = 0$ are related to λ_k , the eigenvalues of the matrix $\mathbf{M}(\alpha, \beta, \kappa)$, by $\sigma_k = \pm(-\lambda_k^{-1})^{1/2}$.

The stability constraint requires that, for given (α, β, κ) , all eigenvalues σ_k should be imaginary, or equivalently, that all eigenvalue reciprocals λ_k^{-1} are real and nonnegative. Clearly, another equivalent condition is that all eigenvalues λ_k are real and nonnegative, interpreting $1/0$ as $+\infty$. Consequently, we define a stability violation function $\tilde{v} : \mathbb{R}^{2n-1} \rightarrow \mathbb{R}_+$ by

$$(\alpha, \beta, \kappa) \mapsto \max \left(\operatorname{Re} \sqrt{-\lambda_k} \right), \quad (4.1)$$

where the maximum is taken over all eigenvalues of $\mathbf{M}(\alpha, \beta, \kappa)$, using the principal square root, hence implying that \tilde{v} cannot take negative values. Besides avoiding the nonlinearity in the reciprocal, the stability violation function \tilde{v} has the virtue that it is continuous, though not Lipschitz continuous, at points in parameter space where a positive eigenvalue λ_k passes through the origin to the negative real axis, and hence \tilde{v} changes continuously from the value zero to a positive value that grows like the square root function at zero. In this case, the parameters cross the divergence boundary, since a conjugate pair of imaginary eigenvalues σ_k coalesce at ∞ and split along the real axis. The function \tilde{v} is also continuous, though not Lipschitz continuous, at points in parameter space where two positive real eigenvalues λ_k, λ_ℓ coalesce and split into a complex conjugate pair, and hence again \tilde{v} increases from zero to a positive quantity that, generically, increases with the square root of the perturbation. In this case, the parameters cross the flutter boundary, because two simple imaginary eigenvalues σ_k, σ_ℓ (and also their conjugates) coalesce on the imaginary axis and split into a complex pair.

We argued in Section 3 that, in the case $n = 2$, the optimal parameter configuration is simultaneously at both the flutter boundary and the divergence boundary, likely with a double eigenvalue λ at zero (equivalently, a quadruple eigenvalue σ at ∞) and, if this is the case, generically, the stability violation function \tilde{v} would grow at nearby parameter configurations with the fourth root of the perturbation.

To compensate for this non-Lipschitz behavior of \tilde{v} , we define a modified stability violation function $v : \mathbb{R}^{2n-1} \rightarrow \mathbb{R}$ by

$$v(\alpha, \beta, \kappa) = \begin{cases} \tilde{v}(\alpha, \beta, \kappa)^\rho, & \tilde{v}(\alpha, \beta, \kappa) \in [0, 1] \\ \rho \tilde{v}(\alpha, \beta, \kappa) - (\rho - 1), & \tilde{v}(\alpha, \beta, \kappa) \in [1, \infty] \end{cases} \quad (4.2)$$

where ρ is a positive integer. In the situations just discussed, the choice $\rho = 2$ is sufficient to make v generically Lipschitz continuous at points where the parameters cross either the divergence or the flutter boundary separately, and $\rho = 4$ is sufficient to make v Lipschitz continuous even when the parameters cross the divergence and flutter boundaries simultaneously, at least at the proposed optimal configuration (3.9), (3.10) for $n = 2$. In our computations, we experimented with choices of ρ from 1 to 5 and we found that $\rho = 4$ gave significantly better results than $\rho < 4$, but that setting $\rho = 5$ made no further improvement. Consequently, we chose to use $\rho = 4$. Note that the specific form of v is chosen so that it does not cause blow-up when $\tilde{v}(\alpha, \beta, \kappa)$ is large, and so that it is continuously differentiable where $\tilde{v}(\alpha, \beta, \kappa) = 1$.

However, what makes this problem particularly difficult is that as any $\beta_i \rightarrow \pi/2$, the coefficient $\mu_i \rightarrow \infty$ in (2.12). Consider the case $n = 2$. We already mentioned in Section 3 that as $\alpha_1 \rightarrow \alpha_1^*$, $\beta_1 \rightarrow \pi/2$ and $\kappa \rightarrow \kappa^*$, we have $\mathbf{M}_{21} \rightarrow \infty$ and $\mathbf{M}_{12} \rightarrow 0$, while \mathbf{M}_{11} is a product of $\tan(\beta_1)$ with a second factor that converges to zero. If this second factor converges to zero more slowly than $(\tan(\beta_1))^{-1}$ does, so that $|\mathbf{M}_{11}| \rightarrow \infty$, a change in its sign causes an eigenvalue λ_k to discontinuously pass through ∞ from the positive real to the negative real axis, implying infinitely large growth in the stability violation v as the parameters cross the divergence boundary. This presents a serious difficulty as we shall see.

In order to solve our optimization problem, we need to impose the stability constraint not only at a given point (α, β, κ) , but also at all points (α, β, ν) with $\nu \in [0, \kappa]$. Although we could construct an approximation to $v(\alpha, \beta, \cdot)$ on the interval $[0, \kappa]$ using approximation software such as Chebfun (63), this is computationally expensive. In our optimization computations, we found that a more effective approach is to impose the stability constraint on a coarse grid of \tilde{q} logarithmically spaced points on $(0, \kappa]$, defining

$$c(\alpha, \beta, \kappa) = \max_{0 \leq j \leq \tilde{q}} (v(\alpha, \beta, \nu_j) : \nu_0 = \kappa, \nu_j = (1 - 2^{-j})\kappa, j = 1, \dots, \tilde{q}) \quad (4.3)$$

and imposing the constraint $c(\alpha, \beta, \kappa) \leq 0$, or equivalently, $c(\alpha, \beta, \kappa) = 0$. Then, after a potential solution is obtained by optimization, we check its stability on a much finer grid of $q \gg \tilde{q}$ uniformly spaced points on $(0, \kappa)$, rejecting it if this test is not passed. We found that using a coarse grid with $\tilde{q} = 10$ points and a fine grid with $q = 10,000$ points worked well, typically with the majority of the solutions obtained by optimization that are feasible for the coarse grid also passing the fine grid test.

We then pose our optimization problem as

$$\begin{aligned}
 & \sup_{\alpha \in \mathbb{R}^{n-1}, \beta \in \mathbb{R}^{n-1}, \kappa \in \mathbb{R}} \kappa \\
 & \text{subject to} \quad c(\alpha, \beta, \kappa) \leq 0, \\
 & \quad 0 \leq \alpha_1 \leq \dots \leq \alpha_{n-1} \leq 1, \\
 & \quad 0 \leq \beta_i \leq \pi/2, \quad i = 1, \dots, n-1,
 \end{aligned} \tag{4.4}$$

This is not an easy problem to solve, since the stability constraint is nonconvex and nonsmooth, as well as discontinuous as $\beta_i \rightarrow \pi/2$. We tackled it using GRANSO (GRAdient-based Algorithm for Non-Smooth Optimization), a recently developed open-source software package for nonsmooth constrained optimization (59, 60).

As its name suggests, the algorithm implemented in GRANSO is based on employing user-supplied gradients. This might seem contradictory since it is intended for nonsmooth optimization problems, but although the constraints are not differentiable everywhere, they are differentiable *almost* everywhere. Specifically, the stability violation function v is differentiable at (α, β, κ) if the following conditions hold:

- (i) the maximum in (4.3) is attained only at one index $j \in (0, \dots, \tilde{q})$
- (ii) the maximum in (4.1) is attained only at one eigenvalue λ_k of $\mathbf{M}(\alpha, \beta, \nu_j)$
- (iii) this eigenvalue λ_k is simple and nonzero.

Thus, evaluating the gradient of v makes sense almost everywhere in parameter space. Of course, the gradient does not vary continuously, but GRANSO is designed to exploit gradient difference information, even near points where the gradient varies discontinuously, building a model of the constraint function on the parameter space using the Broyden-Fletcher-Goldfarb-Shanno (BFGS) quasi-Newton updating method. For more details, see (59), and for application of BFGS in other stability optimization problems, see (64) and the papers cited there.

To derive the gradient of v , we need to differentiate an eigenvalue λ_k with respect to changes in the matrix \mathbf{M} . Let us write $\mathbf{M}(t) = \mathbf{M} + t(\Delta\mathbf{M})$ and let $\lambda(t)$ denote the eigenvalues of $\mathbf{M}(t)$. It is well known (65) that, if $\lambda_k = \lambda(0)$ is a simple eigenvalue of $\mathbf{M} = \mathbf{M}(0)$ satisfying the right and left eigenvector equations $\mathbf{M}u = \lambda u$ and $w^*\mathbf{M}^* = \lambda w^*$, where the asterisk denotes complex conjugate transpose, then

$$\left. \frac{d}{dt} \lambda(t) \right|_{t=0} = \frac{w^*(\Delta\mathbf{M})u}{w^*u}.$$

With this in mind, deriving the gradient of v with respect to the $2n-1$ parameters given by (α, β, κ) is straightforward, employing the chain rule to incorporate the variation in the power function in (4.2), the square root in (4.1), and the formulas (2.13), (2.11) and (2.15).

We now describe our experiments using GRANSO (version 1.6.4), running in MATLAB (release R2020a) on a MacBook Air laptop, to solve (4.4). We used the default choice of parameters with the following exceptions: we set `maxit`, the limit on the iteration count, to 500, and we set the tolerances `opt_tol` and `feas_tol` to zero, to obtain the highest possible accuracy. We added bound constraints on the load variable formulated as $0 \leq \kappa \leq \kappa^{\max}$

with $\kappa^{\max} = 1.1 \times (\kappa_0 + (n-1)\pi)$, that is, with a lower bound of zero and an upper bound set to 10% higher than the proposed optimal value of κ given in (3.12). Since GRANSO may generate iterates violating these bounds or the other bound constraints in (4.4), we defined v to be zero if $\kappa \leq 0$ and replaced β_i in (2.15) by $\text{pi}/2$, the 16 digit rounded value of $\pi/2$, if β_i exceeds $\text{pi}/2$, to avoid the discontinuity in the tangent function at $\pi/2$ (note that $\tan(\text{pi}/2) \approx 1.6 \times 10^{16}$ has the desired positive sign). Because of the difficulty of the problem, we ran the code from many randomly generated starting points, with the initial values for κ , α_i and β_i generated from the uniform distribution on $[0, \kappa^{\max}]$, $[0, 1]$ and $[0, \pi/2]$ respectively, with the α_i then sorted into increasing order.

4.1 Results for $n = 2$

Our analytical discussion of the case $n = 2$ was given in Section 3; the results here strongly support our claim that the optimal configuration is given by (3.9), (3.10). Fig. 9 shows the results obtained by running GRANSO from 1000 randomly generated starting points. Of the 1000 candidate solutions generated by GRANSO, 734 satisfied the bound and coarse grid stability constraints imposed by GRANSO, and of these, 691 also passed the fine grid stability test described above. The top panel in the figure shows the computed optimal loads κ for the best 500 of these feasible solutions, sorted into decreasing order, while the second and third panels show the associated final values of α_1 and β_1 computed by these same 500 runs. The fourth panel shows the eigenvalues of the final associated matrix $\mathbf{M}(\alpha_1, \beta_1, \kappa)$. The highest two final values of κ agree with each other, and with the value $\kappa_0 + \pi$ given in (3.9) and (3.12), to 10 digits. The final values for α_1 and β_1 for these same two best results agree with the value $\kappa_0[\kappa_0 + \pi]^{-1}$ (given in (3.9) and (3.13)) and $\pi/2$, to 10 and 12 digits, respectively. It's also worth noting that the top 100 final values for the computed optimal load agree with $\kappa_0 + \pi$ to 4 digits.

Looking at all four panels of Fig. 9, we see that the top 500 results come in several clearly distinct flavours. The first flavour is exhibited by the best 180 or so runs which all give good approximations to $\kappa_0 + \pi$. However, starting with the 284th result, we find a very different second flavour: many runs find that the computed optimal load is about $\kappa = 4.493$, which agrees with κ_0 , the square root of the critical load for the Dzhaneldze column, to four digits. Clearly, this is a locally maximal value for (4.4); otherwise, it would not be found so frequently. If we look at the associated computed α_1 and β_1 values, usually α_1 is close to zero, but if not, then β_1 is close to zero. It is easily checked that, regardless of the value of β_1 , if $\alpha_1 = 0$ then $\mathbf{M}(\alpha_1, \beta, \kappa_0)$ is the zero matrix, with a double semisimple zero eigenvalue, so this locally optimal parameter configuration, like the apparent globally optimal configuration (3.9), (3.10), is on both the flutter and divergence boundaries. Physically, this corresponds to the mass M_1 being fixed at the clamped end of the column. On the other hand, regardless of the value of α_1 , if $\beta_1 = 0$, then $\mathbf{M}(\alpha_1, \beta_1, \kappa_0)$ has all zero entries except for \mathbf{M}_{12} , and hence has a double zero eigenvalue with a Jordan block. Again, this parameter configuration is on both the flutter and divergence boundaries, and physically, it corresponds to the mass M_1 being zero. Note that the computed eigenvalues for this second flavour of solutions are relatively small.

The third flavour of results is exhibited by the results numbered approximately 180 to 280. In these cases, GRANSO terminated prematurely, without approximating a globally or locally maximal value, and we can see also that, on average, the larger κ is, the closer α_1 is to $\kappa_0[\kappa_0 + \pi]^{-1}$. Investigation of these cases shows that termination occurs because of the

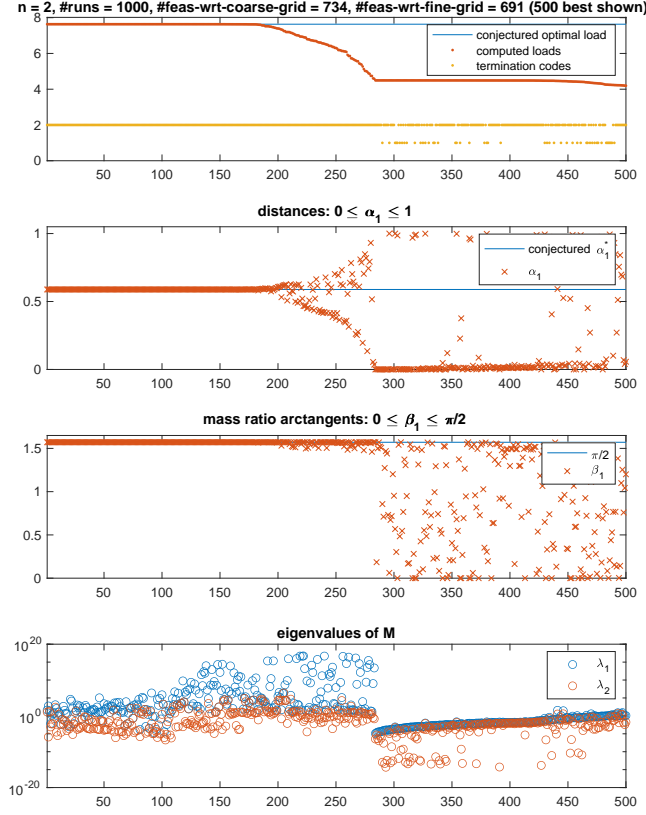


Fig. 9 Summary of results for solving (4.4) with $n = 2$, running GRANSO from 1000 randomly generated starting points. Of the 1000 candidate solutions obtained, 734 satisfied the bound and coarse grid stability constraints imposed by GRANSO, and of these, 691 also passed the fine grid stability test. The top panel in the figure shows the computed optimal loads κ for the best 500 of these feasible solutions, sorted into decreasing order; the top 100 final values all agree with $\kappa_0 + \pi$ to 4 digits, while the top two final values agree with $\kappa_0 + \pi$ to ten digits. The second and third panels show the associated final values of α_1 and β_1 computed by these same 500 runs. The fourth panel shows the eigenvalues of the final associated matrix $\mathbf{M}(\alpha_1, \beta_1, \kappa)$. The computed solutions clearly separate into four flavours; see the text for details.

discontinuity in the stability constraint that we described above. This is also supported by the enormous associated eigenvalues of \mathbf{M} shown in the fourth panel. Note also that as κ increases towards its optimal value, these eigenvalues decrease, but they neither converge to specific values, nor do they become very small. In fact, the matrix \mathbf{M} associated with the best computed optimal κ is

$$\begin{bmatrix} 5.4382 \times 10^1 & -4.0893 \times 10^{-10} \\ 1.3020 \times 10^{12} & -6.8246 \times 10^{-1} \end{bmatrix}$$

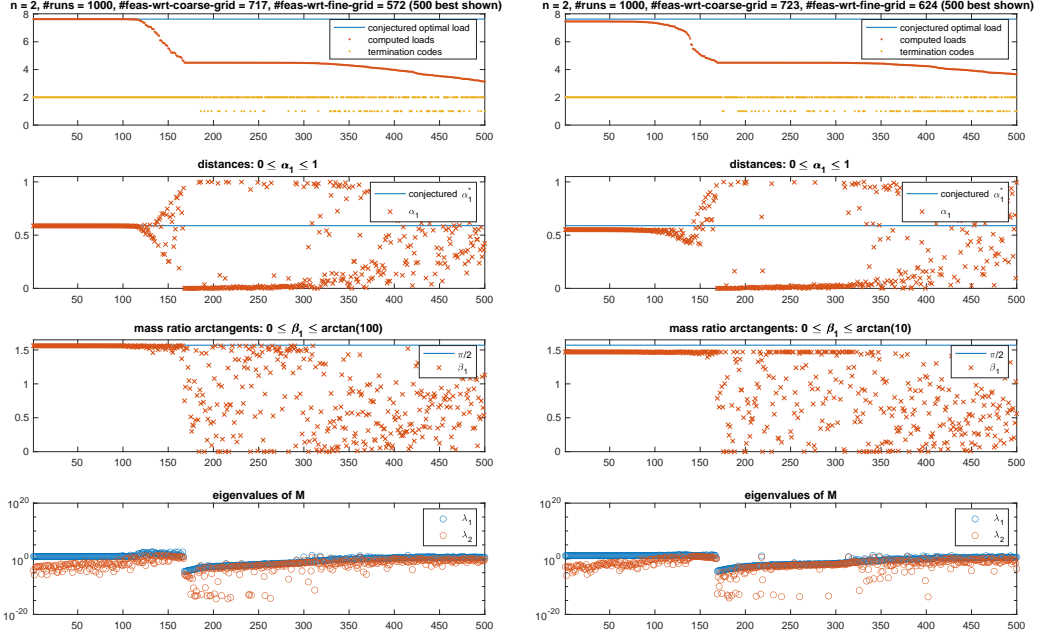


Fig. 10 Solving (4.4) for $n = 2$ with the additional constraint (left) $\beta_1 \leq \arctan(100)$ and (right) $\beta_1 \leq \arctan(10)$. The best computed optimal loads are respectively just 0.1% and 2% lower than the apparent unconstrained supremum $\kappa_0 + \pi$. Note the dramatic reduction in the size of the eigenvalues of the final computed \mathbf{M} compared to Fig. 9. See the caption of Fig. 9 and the accompanying text for more details.

Although its eigenvalues are not close to each other or to zero, they are small relative to the norm of the matrix, and their associated right eigenvectors are almost identical, indicating the nearby presence of a double eigenvalue. Furthermore, the diagonal and upper triangular elements are very small compared to the norm of the matrix, implying that a relatively small perturbation removing them yields a Jordan block with a double zero eigenvalue.

Finally there is a fourth flavour of results: those that did not even reach a good approximation to the locally optimal value κ_0 .

A final comment on Fig. 9: the GRANSO termination codes are plotted at the bottom of the first panel. The value 1 means that GRANSO terminated because the limit of 500 iterations was reached, while the value 2 means that it terminated because it could not find a higher feasible value for the load. Observe that the latter termination always occurred for the runs which approximated the apparent globally optimal load $\kappa_0 + \pi$ well (the first flavour) and the runs that obtained loads higher than κ_0 but terminated without reaching a good approximation to $\kappa_0 + \pi$ (the third flavour). Thus, increasing the iteration limit would not have improved any of these values. On the other hand, the runs that provided a good approximation to the locally maximal value κ_0 (the second flavour) or terminated

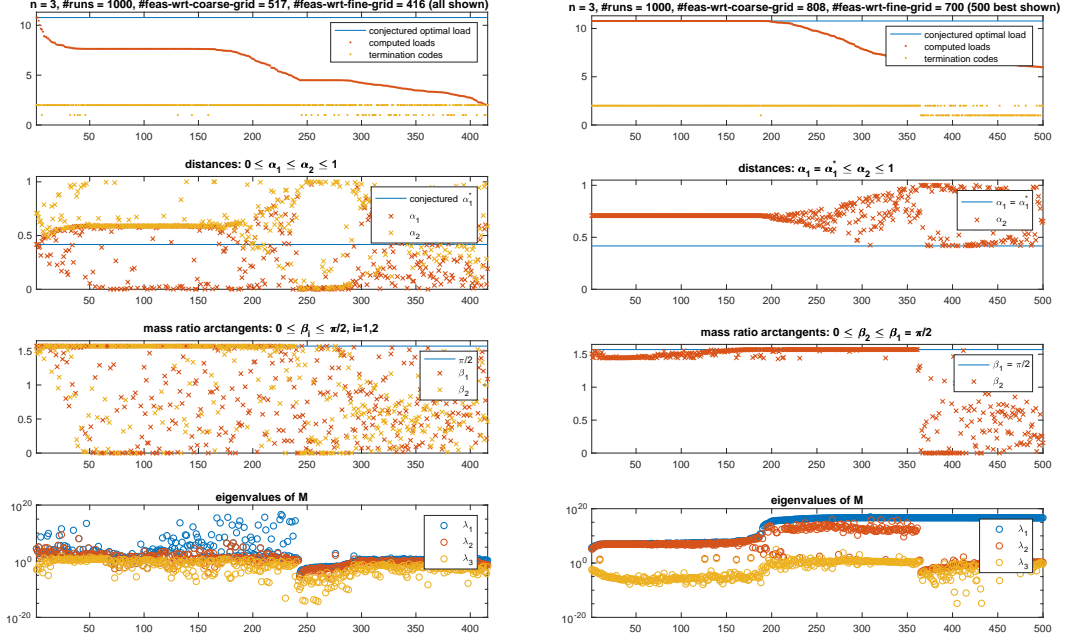


Fig. 11 Solving (4.4) for $n = 3$ with (left) no additional constraints and (right) with the constraints $\alpha_1 = \alpha_1^* = \kappa_0[\kappa_0 + 2\pi]^{-1}$, $\beta_1 = \pi/2$. See the accompanying text for more details.

before reaching that value (the fourth flavour) sometimes, but not always, terminated by exceeding the maximum iteration limit.

The physical interpretation of the proposed supremum (3.9), (3.10) is that the mass M_2 mounted on the free end of the column is zero in the limit $\kappa \rightarrow \kappa^*$ (assuming that M_1 is bounded above). It's interesting to consider what happens if we disallow this case, putting an upper limit on $\mu_1 = M_1/M_2$. Fig. 10 shows the results when we introduce the constraint $\mu_1 \leq 100$ (left) or $\mu_1 \leq 10$ (right) by limiting β_1 to $\arctan(100)$ or $\arctan(10)$ respectively. For $\mu_1 \leq 100$, we now find an optimal load of 7.6287, and for $\mu_1 \leq 10$, we find the optimal load 7.4666, which are respectively just 0.1% and 2% lower than the apparent unconstrained supremum $\kappa_0 + \pi$. The biggest difference we observe from comparing Fig. 10 with Fig. 9 is that the eigenvalues of the final computed \mathbf{M} are now dramatically reduced, from more than 10^{16} to less than 100 and 15 respectively. Thus, we obtain an only slightly reduced optimal load while introducing a much more physically reasonable model with much better numerical properties.

4.2 Results for $n = 3$

The left panel in Fig. 11 shows the results for solving (4.4) for $n = 3$. There are five variables: $\alpha_1, \alpha_2, \beta_1, \beta_2$ and κ . Of the 1000 candidate solutions generated by GRANSO, 517 satisfied the bound and coarse grid stability constraints imposed by GRANSO, and of these, 416 passed the fine grid test. We see immediately that the problem for $n = 3$ is significantly harder than for

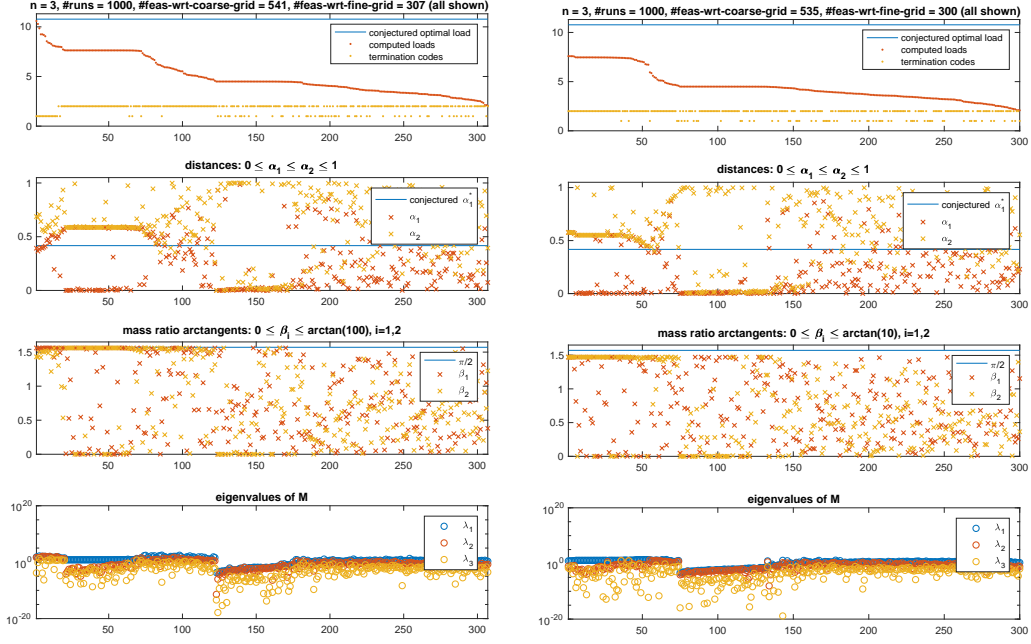


Fig. 12 Solving (4.4) for $n = 3$ with the additional constraints (left) $\beta_i \leq \arctan(100)$, $i = 1, 2$ and (right) $\beta_i \leq \arctan(10)$, $i = 1, 2$.

$n = 2$, with not many runs approximating the conjectured optimal value well. Nonetheless, the two best runs generate $\kappa \approx 1.0776$, which agrees with the conjectured optimal value $\kappa_0 + 2\pi$ to five digits. These two runs also generate $\alpha_1 \approx 0.4169$ and $\beta_1 \approx 1.570796$ which agree with the conjectured optimal values $\alpha_1^* = \kappa_0[\kappa_0 + 2\pi]^{-1}$ and $\pi/2$ to 4 and 7 digits, respectively. The right panel in the same figure shows the results when we fix $\alpha_1 = \alpha_1^*$ and $\beta_1 = \pi/2$ (the 16 digit rounded value of $\pi/2$) and optimize over the remaining three variables α_2 , β_2 and κ . Then the best two runs generate κ agreeing with $\kappa_0 + 2\pi$ to 12 digits, and the best 100 runs agree with this to 10 digits. Together, the results reported in the left and right panels of Fig. 11 make a convincing argument that the values shown in (3.12) and (3.13) are indeed the supremal value κ^* and the corresponding limiting value α_1^* when $n = 3$, and that the corresponding limiting value β_1^* is again $\pi/2$. Although we do not have a conjectured formula for α_2^* , its computed optimal value is 0.7085. Furthermore, the limiting value β_2^* is again apparently $\pi/2$, meaning the mass ratio $\mu_2 = M_2/M_3 \rightarrow \infty$ as $\kappa \rightarrow \kappa^*$, which indeed must be the case assuming the limiting value of M_2 is nonzero and M_1 is bounded above, since then $\beta_1 \rightarrow \pi/2$ implies that $M_3 \rightarrow 0$.

Fig. 12 shows the results when we introduce the mass ratio constraint $\mu_i \leq 100$ (left) or $\mu_i \leq 10$ (right) by limiting $\beta_i \leq \arctan(100)$, $i = 1, 2$ or $\beta_i \leq \arctan(10)$, $i = 1, 2$ respectively. For $\mu_i \leq 100$, we now find an optimal load of 10.589, which is only 0.5% lower than $\kappa_0 + 2\pi$. However, when we constrain $\mu_i \leq 10$, the best optimal load found is only 7.59,

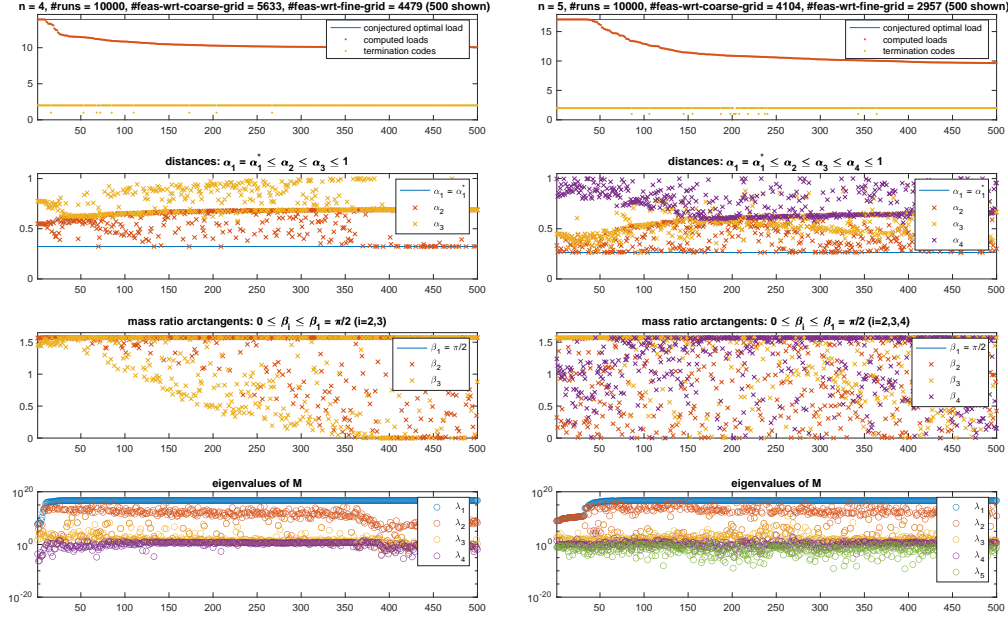


Fig. 13 (Left) solving (4.4) for $n = 4$ with the constraints $\alpha_1 = \alpha_1^* = \kappa_0[\kappa_0 + 3\pi]^{-1}$, $\beta_1 = \pi/2$ and (right) solving (4.4) for $n = 5$ with the constraints $\alpha_1 = \alpha_1^* = \kappa_0[\kappa_0 + 4\pi]^{-1}$, $\beta_1 = \pi/2$.

which is a 30% reduction from $\kappa_0 + 2\pi$. When we repeat these runs with 10,000 starting points instead of 1000, these numbers are only slightly improved.

4.3 Results for $n = 4$ and $n = 5$

The optimization problem is so much harder for $n = 4$ and $n = 5$ that we needed 10,000 starting points to get good results, even when we set α_1 to its conjectured optimal value in (3.13) and β_1 to $\pi/2$, optimizing over the remaining 5 and 7 variables, respectively. The results are shown in the left and right panels of Fig. 13. For $n = 4$, the best 5 results agree with our conjectured optimal load $\kappa_0 + 3\pi$ to 8 digits, while for $n = 5$, the best 25 results agree with $\kappa_0 + 4\pi$ to 7 digits. These results strongly support our conjecture regarding the supremal load κ for n masses given in (3.12).

5. Concluding Remarks

We believe we have made a convincing case that the supremal load for the strongest stable massless column with a follower load and n relocatable masses is, in the dimensionless model defined in Section 2, $\kappa_0 + (n - 1)\pi$, where κ_0 is the smallest positive root of $\tan(\kappa) = \kappa$. This conjecture has not previously appeared in the literature as far as we know, except in the case $n = 1$ where it has been known to be true for decades (6). We have given a detailed analytical derivation of this result for $n = 2$, and presented extensive computational results that support it for $n = 2, 3, 4, 5$, using numerical nonsmooth optimization.

With this model problem effectively solved, we believe it would be interesting to apply our nonsmooth optimization techniques to more realistic columns with follower loads (29), such as the Beck, Pflüger and Leipholz columns with a single free end as well as to free-free beams both with distributed and concentrated masses to get new insights about the nature of the optimal solution to these long-standing optimization problems. We believe it is also important to consider extending traditional stability constraints to more robust stability constraints based on pseudospectra (66), a topic that is beyond the scope of this paper.

Acknowledgements. The authors thank Tim Mitchell, the author of GRANSO, for many helpful discussions and suggestions regarding the formulation of the stability constraint. They also thank the London Mathematical Society for supporting the second author's visit to Northumbria through the Scheme 4 Research in Pairs grant No 41820. The second author was supported in part by the U.S. National Science Foundation Grant DMS-2012250.

References

1. Beck M (1952) Die Knicklast des einseitig eingespannten, tangential gedrückten Stäbes. *Z angew Math Mech* 3:225–228.
2. Carr J and Malhardeen M Z M (1979) Beck's problem. *SIAM J Appl Math* 37:261–262.
3. Sugiyama Y, Langthjem M, Katayama K (2019) Dynamic stability of columns under nonconservative forces: theory and experiment. *Solid mechanics and its applications*. Vol 255 Springer, Berlin.
4. Ziegler H (1953) Linear elastic stability. A critical analysis of methods, First part. *ZAMP Z angew Math Phys* 4:89–121.
5. Ziegler H (1953) Linear elastic stability. A critical analysis of methods, Second part. *ZAMP Z angew Math Phys* 4:167–185.
6. Bolotin V V (1963) *Nonconservative problems of the theory of elastic stability*. Pergamon Press, Oxford.
7. Kirillov O N (2013) *Nonconservative stability problems of modern physics*. De Gruyter series in mathematical physics. Vol 14 De Gruyter, Berlin, Boston.
8. Bayly P V and Dutcher S K (2016) Steady dynein forces induce flutter instability and propagating waves in mathematical models of flagella. *J R Soc Interface* 13:20160523.
9. De Canio G, Lauga E, Goldstein R E (2017) Spontaneous oscillations of elastic filaments induced by molecular motors. *J R Soc Interface* 14:20170491.
10. Fatehiboroujeni S, Gopinath A, Goyal S (2021) Three-dimensional nonlinear dynamics of prestressed active filaments: Flapping, swirling, and flipping. *Phys Rev E* 103; 013005.
11. Zhu L, Stone H A (2019) Propulsion driven by self-oscillation via an electrohydrodynamic instability. *Phys Rev Fluids* 4:061701.
12. Zhu L, Stone H A (2020) Harnessing elasticity to generate self-oscillation via an electrohydrodynamic instability. *J Fluid Mech* 888:A31
13. Sugiyama Y, Langthjem M, Ryu B-J (1999) Realistic follower forces. *J Sound Vibr* 225:779–782.
14. Sugiyama Y, Langthjem M, Ryu B-J (2002) Beck's column as the ugly duckling. *J Sound Vibr* 254:407–410.
15. Sundararajan C (1975) Optimization of a nonconservative elastic system with stability constraint. *J Opt Theory Appl* 16(3/4):355–378.

16. Park Y P, Mote C D (1985) The maximum controlled follower force on a free-free beam carrying a concentrated mass. *J Sound Vibr* 98(2):247–256.
17. Kirillov O N, Seyranian A P (1998) Optimization of stability of a flexible missile under follower thrust. *AIAA Paper* 98-4969:2063–2073.
18. Sugiyama Y, Matsuike J, Ryu B-T, Katayama K, Kinoi S, Enomoto N (1995) Effect of concentrated mass on stability of cantilevers under rocket thrust. *AIAA J.* 33(3):499–503.
19. Sugiyama Y, Langthjem M A, Iwama T, Kobayashi M, Katayama K, Yutani H (2012) Shape optimization of cantilevered columns subjected to a rocket-based follower force and its experimental verification. *Struct. Multidisc. Opt.* 46:829–838.
20. Bigoni D, Noselli G (2011) Experimental evidence of flutter and divergence instabilities induced by dry friction. *J Mech Phys Sol* 59:2208–2226.
21. Bigoni D, Kirillov O N, Misseroni D, Noselli G, Tommasini M (2018) Flutter and divergence instability in the Pflüger column: Experimental evidence of the Ziegler destabilization paradox. *J Mech Phys Sol* 116:99–116.
22. Bigoni D, Misseroni D, Tommasini M, Kirillov O N, Noselli G (2018) Detecting singular weak-dissipation limit for flutter onset in reversible systems. *Phys Rev E* 97(2):023003.
23. Pflüger A (1955) Zur Stabilität des tangential gedrückten Stäbes. *Z Angew Math Mech* 35(5):191.
24. Deineko K S, Leonov M Ia (1955) A dynamic method for the investigation of the stability of a compressed bar. *Prikl Mat Mekh* 19:738–744.
25. Tommasini M, Kirillov O N, Misseroni D, Bigoni D (2016) The destabilizing effect of external damping: Singular flutter boundary for the Pflüger column with vanishing external dissipation. *J Mech Phys Sol* 91:204–215.
26. Oran C (1972) On the significance of a type of divergence. *J Appl Mech* 39:263–265.
27. Sugiyama Y, Kashima K, Kawagoe H (1976) On an unduly simplified model in the non-conservative problems of elastic stability. *J Sound Vib* 45(2):237–247.
28. Chen L W, Ku D W (1992) Eigenvalue sensitivity in the stability analysis of Beck’s column with a concentrated mass at the free end. *J Sound Vib* 153(3):403–411.
29. Gajewski A, Zyczowski M (1988) Optimal structural design under stability constraints. Kluwer, Dordrecht.
30. Claudon J L (1975) Characteristic curves and optimum design of two structures subjected to circulatory loads. *J. de Mecanique* 14(3):531–543.
31. Hanaoka M, Washizu K (1980) Optimum design of Beck’s column. *Comp Struct* 11(6):473–480.
32. Kounadis A N, Katsikadelis J T (1980) On the discontinuity of the flutter load for various types of cantilevers. *Intern J Solids Struct* 16:375–383.
33. Bogacz R, Frischmuth K (2018) On optimality of column geometry. *Arch Appl Mech* 88:317–327.
34. Mahrenholtz O, Bogacz R (1981) On the shape of characteristic curves for optimal structures under non-conservative loads. *Arch Appl Mech* 50:141–148.
35. Langthjem M A, Sugiyama Y (2000) Optimum design of cantilevered columns under the combined action of conservative and nonconservative loads Part I: The undamped case. *Comp Struct* 74(4):385–398.
36. Ringertz U T (1994) On the design of Beck’s column. *Struct Opt* 8(2):120–124.
37. Temis Yu M, Fedorov I M (2007) Shape optimization of nonconservatively loaded beams

- with a stability criterion. *Probl Strength Plast* 69:24–37.
38. Kirillov O N, Seyranian A P (2002) Metamorphoses of characteristic curves in circulatory systems. *J Appl Math Mech* 66(3):371–385.
 39. Kirillov O N, Seyranian A P (2002) A non-smooth optimization problem. *Moscow Univ Mech Bulletin* 57(3):1–6.
 40. O'Reilly O M, Malhotra N K, Namachchivaya N S (1996) Some aspects of destabilization in reversible dynamical systems with application to follower forces. *Nonlin Dynamics* 10:63–87.
 41. Seyranian A P, Kirillov O N (2001) Bifurcation diagrams and stability boundaries of circulatory systems. *Theor Appl Mech* 26: 135–168.
 42. Kirillov O N, Seyranian A P (2004) Collapse of the Keldysh chains and stability of continuous non-conservative systems. *SIAM J Appl Math* 64(4):1383–1407.
 43. Kirillov O N, Overton M L (2013) Robust stability at the swallowtail singularity. *Frontiers in Physics* 1: 24.
 44. Kirillov O N (2011) Singularities in structural optimization of the Ziegler pendulum. *Acta Polytechn* 51(4):32–43.
 45. Langthjem M A, Sugiyama Y (1999) Optimum shape design against flutter of a cantilevered column with an end-mass of finite size subjected to a non-conservative load. *J Sound Vibr* 226(1):1–23.
 46. Katsikadelis J T, Tsiatas G C (2007) Optimum design of structures subjected to follower forces. *Intern J Mech Sci* 49:1204–1212.
 47. Kordas Z, Zyczkowski M (1963) On the loss of stability of a rod under a super-tangential force. *Arch Mech Stos* 1(15):7–31.
 48. Lee H P (1997) Flutter of a cantilever rod with a relocatable lumped mass. *Comput Methods Appl Mech Engrg* 144:23–31.
 49. Hauger W (1967) Bemerkungen zu dem Einfluss der Massenverteilung bei nichtkonservativen Stabilitätsproblemen elastischer Stäbe. *Ing.-Arch.* 35:283–291.
 50. Leipholz H, Lindner G (1970) Über den Einfluss der Massenverteilung auf das nichtkonservative Knicken von Stäben. *Ing.-Arch.* 39:187–194.
 51. Kapoor R N, Leipholz H (1974) Stability analysis of a damped polygenic systems with relocatable mass along its length. *Ing.-Arch* 43:233–239.
 52. Kapoor R N, Leipholz H (1974) On mass distribution, rotary inertia and external damping of a viscoelastic polygenic system. *Z Angew Math Mech* 54(3):205–208.
 53. Kounadis A N (1977) Stability of elastically restrained Timoshenko cantilevers with attached masses subjected to a follower force. *ASME J Appl Mech* 44(4):731–736.
 54. Cazzolli A, Dal Corso F, Bigoni D (2020) Non-holonomic constraints inducing flutter instability in structures under conservative loadings. *J. Mech. Phys. Solids* 138, 103919.
 55. Bazant Z P, Cedolin L (2010) Stability of structures: elastic, inelastic, fracture and damage theories. World Scientific, Singapore.
 56. Kagan-Rosenzweig L M (2001) Quasi-static approach to non-conservative problems of the elastic stability theory. *Int J Solids Struct* 38:1341–1353.
 57. Ingerle K (2013) Stability of massless non-conservative elastic systems. *J Sound Vibr* 332:4529–4540.
 58. Kagan-Rosenzweig L M (2014) Topics in nonconservative stability theory. (St.-Petersburg Univesity Press, St. Petersburg. In Russian.

59. Curtis F E, Mitchell T, Overton M L (2017) A BFGS-SQP method for nonsmooth, nonconvex, constrained optimization and its evaluation using relative minimization profiles. *Optim Methods Softw* 32:148–181.
60. Mitchell T (2020) GRANSO: GRAdient-based Algorithm for Non-Smooth Optimization. <http://www.timmitchell.com/software/GRANSO/>
61. Gallina P (2003) About the stability of non-conservative undamped systems. *J. Sound Vibr.* 262:977–988.
62. Bulatovic R M (2011) A sufficient condition for instability of equilibrium of non-conservative undamped systems. *Phys Lett A* 375:3826–3828.
63. Driscoll T A, Hale N, Trefethen L N (2014), *Chebfun Guide*. Pafnuty Publications, Oxford.
64. Overton M L (2014) Stability optimization for polynomials and matrices. In: *Nonlinear Physical Systems: Spectral Analysis, Stability and Bifurcations* (O. Kirillov, D. Pelinovsky, eds.), 351–375. John Wiley & Sons Inc., New York.
65. Greenbaum A, Li R-C, Overton M L (2020). First-order perturbation theory for eigenvalues and eigenvectors. *SIAM Rev* 62: 463–482.
66. Trefethen L N, Embree M (2006) *Spectra and pseudospectra: the behavior of nonnormal matrices and operators*. Princeton University Press.

APPENDIX A

Pflüger's column

To model the Pflüger column we consider an elastic beam of length l , with Young's modulus E and mass per unit length m , clamped at one end and loaded by a tangential follower force P at the other end, where a point mass M is mounted. The moment of inertia of a cross-section of the column is denoted by I . Small lateral vibrations of the Pflüger column near the undeformed equilibrium are described by the linear partial differential equation (23, 25)

$$EI \frac{\partial^4 y}{\partial s^4} + P \frac{\partial^2 y}{\partial s^2} + m \frac{\partial^2 y}{\partial t^2} = 0 \quad (\text{A.1})$$

where $y(s, t)$, is the amplitude of the vibrations and $s \in [0, l]$ is a coordinate along the column. At the clamped end ($s = 0$) equation (A.1) satisfies the boundary conditions

$$y = 0, \quad \frac{\partial y}{\partial s} = 0, \quad s = 0, \quad (\text{A.2})$$

while at the loaded end ($s = l$), the boundary conditions are

$$EI \frac{\partial^2 y}{\partial s^2} = 0, \quad EI \frac{\partial^3 y}{\partial s^3} = M \frac{\partial^2 y}{\partial t^2}, \quad s = l. \quad (\text{A.3})$$

Introducing the dimensionless quantities

$$\xi = \frac{s}{l}, \quad \tau = \frac{t}{l^2} \sqrt{\frac{EI}{m}}, \quad p = \frac{Pl^2}{EI}, \quad \mu = \frac{M}{ml}, \quad (\text{A.4})$$

and separating the time variable through $y(\xi, \tau) = lf(\xi) \exp(\lambda\tau)$, we obtain the dimensionless boundary eigenvalue problem

$$\partial_\xi^4 f + p \partial_\xi^2 f + \lambda^2 f = 0, \quad (\text{A.5})$$

$$\begin{aligned} \partial_\xi^2 f(1) &= 0, \quad \partial_\xi^3 f(1) = \mu \lambda^2 f(1), \\ f(0) &= 0, \quad \partial_\xi f(0) = 0 \end{aligned} \quad (\text{A.6})$$

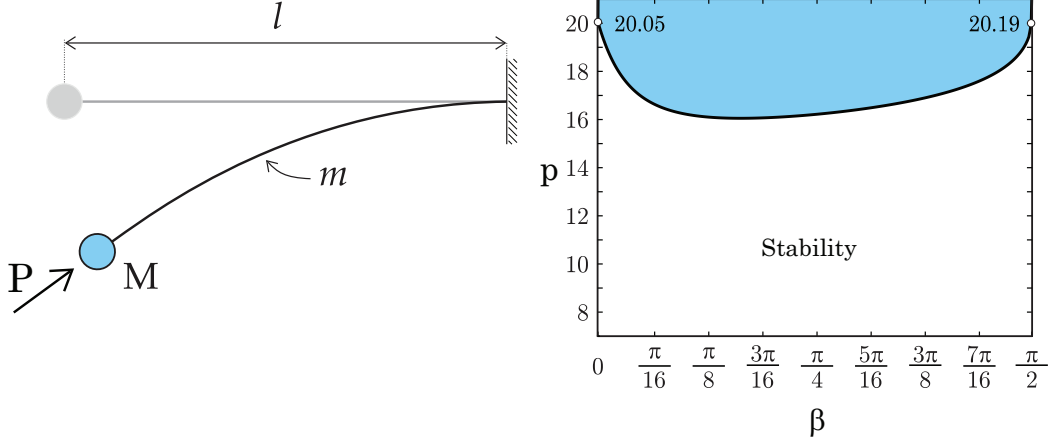


Fig. A The Pflüger column and its stability diagram. The ratio of the end mass to the mass of the column, $\mu = M/(ml)$, is parameterized by $\mu = \tan \beta$. The Beck column corresponds to the vanishing end mass ($M = 0$, so $\beta = 0$) and the massless Pflüger column (or Dzhanelidze's column (6)) to the vanishing mass of the rod ($m = 0$, so $\beta = \pi/2$). The vertical axis of the stability diagram shows the dimensionless load $p = \frac{Pl^2}{EI}$, where E is Young's modulus, I is the moment of inertia of a cross-section of the column and l is the length of the column.

defined on the interval $\xi \in [0, 1]$. A solution to the equation (A.5) with boundary conditions (A.6) is (23, 25)

$$f(\xi) = A(\cosh(g_2\xi) - \cos(g_1\xi)) + B(g_1 \sinh(g_2\xi) - g_2 \sin(g_1\xi)) \quad (\text{A.7})$$

with

$$g_{1,2} = \sqrt{\frac{\sqrt{p^2 - 4\lambda^2} \pm p}{2}},$$

where the subscripts 1 and 2 correspond to the signs $+$ and $-$, respectively. Imposing the boundary conditions (A.6) on the solution (A.7) yields the characteristic equation $\Delta(\lambda) = 0$ for the determination of the eigenvalues λ , where

$$\Delta(\lambda) = \Delta_1 - \Delta_2 \mu \lambda^2$$

and

$$\begin{aligned} \Delta_1 &= g_1 g_2 (g_1^4 + g_2^4 + 2g_1^2 g_2^2 \cosh g_2 \cos g_1 + g_1 g_2 (g_1^2 - g_2^2) \sinh g_2 \sin g_1) \\ \Delta_2 &= (g_1^2 + g_2^2) (g_1 \sinh g_2 \cos g_1 - g_2 \cosh g_2 \sin g_1). \end{aligned} \quad (\text{A.8})$$

Parameterizing the mass ratio in (A.4) by $\mu = \tan \beta$ with $\beta \in [0, \pi/2]$ enables the exploration of all possible ratios $\mu = M/(ml)$ of the end mass to the mass of the column from zero ($\beta = 0$) to infinity ($\beta = \pi/2$). The former case, without the end mass, corresponds to the Beck column, whereas the latter corresponds to a massless rod with an end mass, which is known as the Dzhanelidze column (6).

It is well-established that the uniform Beck column is stable against flutter if the dimensionless follower force, p , is such that $0 \leq p \lesssim 20.05$, (1, 2, 6, 7). In contrast, the Dzhanelidze column becomes unstable at $p \approx 20.19$, which is the smallest positive root of the equation (6)

$$\tan \sqrt{p} = \sqrt{p}. \quad (\text{A.9})$$

These values, representing two extreme situations, are connected by a marginal stability curve in the (β, p) -plane (**6**, **23**, **25**, **26**, **27**, **28**); see the right panel of Fig. A.

For every fixed value $\beta \in [0, \pi/2)$, the Pflüger column loses stability via flutter when an increase in p causes the imaginary eigenvalues of two different modes to approach each other and merge into a double imaginary eigenvalue with a Jordan block (i.e., with algebraic multiplicity two and geometric multiplicity one). When p crosses the threshold, the double eigenvalue splits into two complex eigenvalues, one with positive real part, which determines a flutter-unstable mode.

At $\beta = \pi/2$ the stability boundary of the Pflüger column has a vertical tangent and the type of instability changes from flutter to divergence, i.e., non-oscillatory growth of a mode corresponding to a positive real eigenvalue, for $p \gtrsim 20.19$; see (**6**, **26**, **27**).